Article

A Discrete-Continuous Method for Predicting Thermochemical Phenomena in a Cement Kiln and Supporting Indirect Monitoring

Edoardo Copertaro[1,*]**, Paolo Chiariotti**[2]**, Alvaro Antonio Estupinan Donoso**[1]**, Nicola Paone**[2]**, Bernhard Peters**[1]**, and Gian Marco Revel**[2]

1 Université du Luxembourg, Faculté des Sciences, de la Technologie et de la Communication, Avenue de l'Université, L-4365, Esch-sur-Alzette, Luxembourg
2 Università Politecnica delle Marche, Dipartimento di Ingegneria Meccanica e Scienze Matematiche, Via Brecce Bianche 12, 60131, Ancona, Italy
*E-mail: edoardo.copertaro@uni.lu (Corresponding author)

Abstract. Thermochemical phenomena involved in cement kilns are still not well understood because of their complexity, besides technical difficulties in achieving direct measurements of critical process variables. This article addresses the problem of their comprehensive numerical prediction. The presented numerical model exploits Computational Fluid Dynamics and Finite Difference Method approaches for solving the gas domain and the rotating wall, respectively. The description of the thermochemical conversion and movement of the powder particles is addressed with a Lagrangian approach. Coupling between gas, particles and the rotating wall includes momentum, heat and mass transfer. Three-dimensional numerical predictions for a full-size cement kiln are presented and they show agreement with experimental data and benchmark literature. The quality and detail of the results are believed to provide a new insight into the functioning of a cement kiln. Attention is paid to the computational burden of the model and a methodology is presented for reducing the time-to-solution and paving the way for its exploitation in quasi-real-time, indirect monitoring.

Keywords: Cement kiln, computational fluid dynamics, discrete element method.

1. Introduction

Cement represents the fundamental material in many building and civil engineering applications. Among several types, the most common is Portland, which is made of a mixture of gypsum and clinker. The clinker production process includes a pyro-processing treatment taking place inside dry kilns equipped with five or six cyclone preheaters and a precalciner. The operation is dramatically energy-intensive, with a heat use of 2900-3300 MJ per ton of clinker [1]. Here the raw material comes from the grinding operation in the state of powder particles; a first heating up to about 870 °C is performed inside the preheaters then the precalciner; subsequently the material, almost completely calcined, enters the dry kiln, where its temperature is raised up to 1400-1500 °C; follows a rapid cooling, which prevents the decomposition of metastable phases.

The dry kiln is a large reactor consisting of a rotating tube with an outer steel shell and inner refractory lining. It is typically inclined 1-3 degrees (longitudinal axis with respect to horizontal line) and rotates at 1-5 rpm [1]. The typical length-to-diameter ratio is 16:1-13:1 and recently even shorter [1]. The particles of the material bed flow inside the kiln and exchange heat with the rotating wall and a hot countercurrent air flow i.e. the freeboard gas, whose initial enthalpy is provided by heat recovery from the cooling stage and fuel burning. As a result, the temperature of the material is raised while it moves towards the exit and several chemical conversions take place until clinker is obtained. The thermochemical phenomena occurring inside the material bed are heavily affected by its powder state [2]. Indeed, the in-plane recirculation of the particles, which is due to the dragging of the rotating wall, produces a redistribution of heat within the material bed and helps reducing the inhomogeneity of properties in the final product.

A highly aggressive environment and physical inaccessibility prevent the direct monitoring of many process variables inside a cement kiln [3]. The consequent lack of real data impacts negatively on the understanding and optimization of the system, which accounts for a major fraction of the plant heat losses [4]. Nevertheless, process optimization is a key target for the global cement industry, which is facing constantly increasing coal prices and always more demanding environmental regulations [5, 6]. Numerical models could represent effective tools for filling the knowledge gap: indeed, their comprehensive predictions could constitute the theoretical support for new indirect monitoring approaches based on soft sensing [7], as well as optimization-oriented control strategies [8].

Many authors have extensively investigated the movement of particles inside rotary kilns. In [9–13], particles motion in rotating drums has been investigated by means of optical fibers, magnetic resonance imaging, high-speed cameras and positron emission tracking, respectively. In [2, 14], analytical models have been presented, for predicting the flow of granular materials inside rotating drums: the governing equations are similar to those derived for conventional fluids, but conservation of the kinetic energy is also accounted in the formulation along with momentum and mass transport. In [15], an analytical prediction of the particles flow has been obtained for the specific case of rolling-mode operated drums. Discrete Element Method (DEM) has been increasingly used for predicting particles movement in rotating drums [16–22], following the breakthrough of higher computing power. Its undoubted advantage respect to other methods like stochastic or empirical is the possibility of obtaining a deterministic estimation of the trajectory of each particle. However, DEM presents high computation requirements which grow as the number of particles increases, therefore preventing the application to many large-scale scenarios in industry unless periodic boundaries and/or agglomeration [23] are used for limiting both the size of the domain and the total number of particles.

Different authors have discussed numerical studies of the thermochemical phenomena occurring inside cement kilns. A 1D model based on heat and mass balances is presented in [24]. The same model has been resumed with minor changes by other authors [25, 26]. CFD (Computational Fluid Dynamics) studies of the freeboard gas and mostly focused on the burner design are reported in [27–32]. In [33] it is presented the first complete model of a cement kiln, which includes a CFD study of the freeboard gas along with numerical predictions of the material bed and the rotating wall, as well. Analogous models have been lately presented in [34, 35]. However, in these studies the accurate representation of the freeboard gas contrasts with strong assumptions over the material bed, whose flow is described as the rigid translation of a continuum along the axial direction of the kiln, regardless its real powder state and the consequent in-plane recirculation.

In [36] it is presented a retrospective review of mathematical models for the representation of a porous medium and the related heat and mass transfer coefficients by means of an equivalent continuum. These constitute the theoretical basis of unresolved CFD-DEM methods like those reported in [37–39] and others.

The present contribution discusses the application of an eXtended Discrete Element Method (XDEM) approach for predicting the thermochemical phenomena occurring in a dry kiln for clinker production.

XDEM is a numerical framework based on a coupled CFD-DEM method. The model includes: a Lagrangian prediction of the particles flow and the heat exchange between particles, along with heat and mass transport inside particles and their chemical conversions and morphology changes; a CFD prediction of the gas domain including fuel transport and its combustion; an FDM (Finite Difference Method) approach for solving the heat equation on the rotating wall. Particles-gas coupling includes mass, momentum and convective heat transfer. Particles-wall conductive and gas-wall convective heat transfer are included in the formulation, as well. A simplified resistance model is included for predicting the gas-wall-particles radiative heat transfers. XDEM has already been tested in the prediction of the phenomena involved in several industrial processes including pyrolysis [40], metal manufacturing [41, 42], drying [43, 44], $CaCO_3$ decarbonation [45, 46] and others [47–49].

The model presented exploits several assumptions for limiting the computation burden. These will be detailed in the following discussion. An effective numerical methodology is presented, for reducing the time-to-solution to the length scale of hours. The computation efficiency of the numerical tool is expected to allow its integration into the plant SCADA architecture as an indirect monitoring tool, useful for backup and/or integration of the hardware distributed sensors.

The predictions discussed in this paper are consistent with experimental and literature data. To the best knowledge of the authors, the present study is the first application of a combined Eulerian-Lagrangian method to the prediction of the phenomena involved in the clinker production.
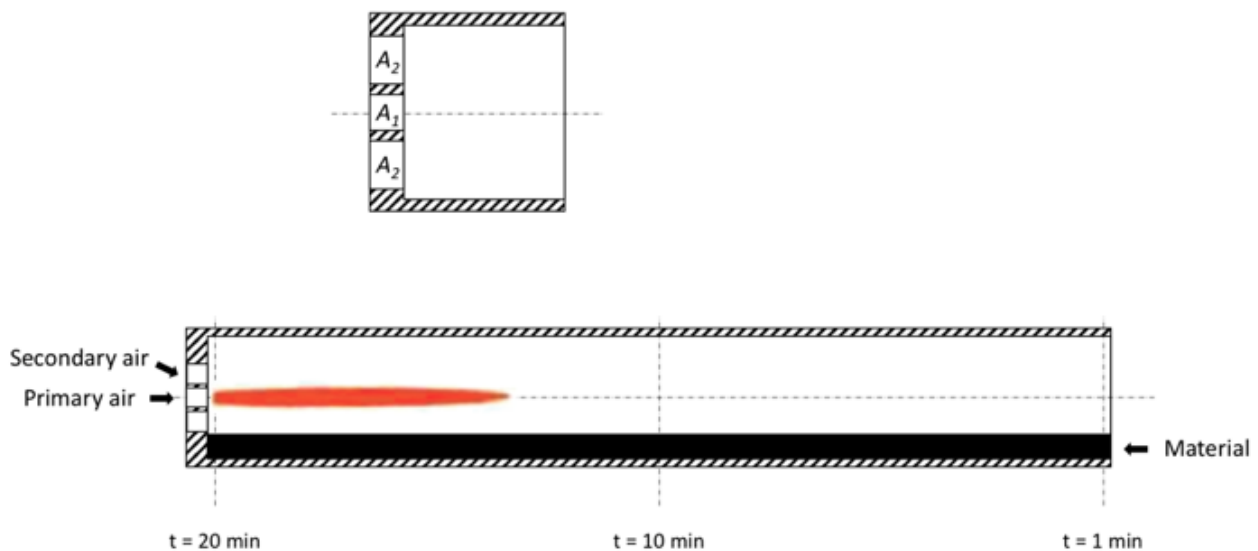
2. The Real Kiln

Fig. 1.   Kiln geometry, detail of air-intake and positions of DEM domain at different times.

A real dry kiln for clinker production (length: 54 m; internal radius: 2.1 m; external radius: 2.3 m) has been considered. Its geometry is depicted in Fig. 1. The kiln is operated at a filling level of 15 % and processes a total mass flow of 140 t/h. The material enters the kiln at a temperature of 1220 K. The chemical composition of a fresh sample, i.e. at room temperature, is reported in Table 1. Loss on Ignition (LOI) is defined as the mass loss of a fresh sample ignited at 1173 to 1273 K. This is consequent to the decarbonation process of limestone into calcium oxide ($CaCO_3 \rightarrow CaO + CO_2$). As typical of dry kilns, the one considered here receives the input material almost completely calcined with a decarbonation percentage at 98 %, therefore LOI occurring inside the kiln is negligible. The kiln rotates at 4 rpm and is tilted 2 degrees. The retention time (i.e. the mean time spent by the material inside the kiln) is 20 min. The hot gas moves countercurrent to the material bed and the total flow includes: the secondary air from heat recovery, which enters at a rate and temperature of 80000 m3/h and 950 K, respectively; the primary air with the coal particles in suspension, which is injected through the burner at room temperature and at a rate of 5700 m3/h. The kiln is operated at a depression of -200 Pa respect to the environment, in order to force the extraction of the exhaust gases. The set of measurements include the flame temperature (in the range of 2073-2173 K), the mean temperature

of the material in the sintering zone (1733 K), the mean temperature of the material at the exit (1673 K) and the speed of the gas at the exhaust (15-17 m/s).

Table 1.   Chemical composition of a fresh sample.

Specie	Mass fraction
SiO_2	0.14
Al_2O_3	0.03
Fe_2O_3	0.02
CaO	0.43
MgO	0.03
LOI	0.35

Cement kilns are giant reactors that represent some of the largest-size, moving machineries ever built. Consequently, the CFD-DEM representation must deal with a dramatically broad range of scales, being the characteristic size of clinker lumps in the order of centimeters [50]. A numerical simulation that brutally addresses the kiln at the whole size is clearly impossible due to the excessive computation burden. Therefore, simplifications have been made and they are discussed in the following subsections.

3.   The Model

3.1.   DEM Approach for the Powder Domain

Two periodic boundaries orthogonal to the kiln axis have been imposed, spaced of 0.4 m each other. The thin slice constituting the DEM domain is depicted in Fig. 2, together with the frame of reference that will be used from here on. The volume has been filled with 4000 spherical particles with a diameter of 0.06 m, providing the filling level required. The diameter of the particles and the spacing between the periodic boundaries have been chosen by upscaling the analogous setup reported in [22].
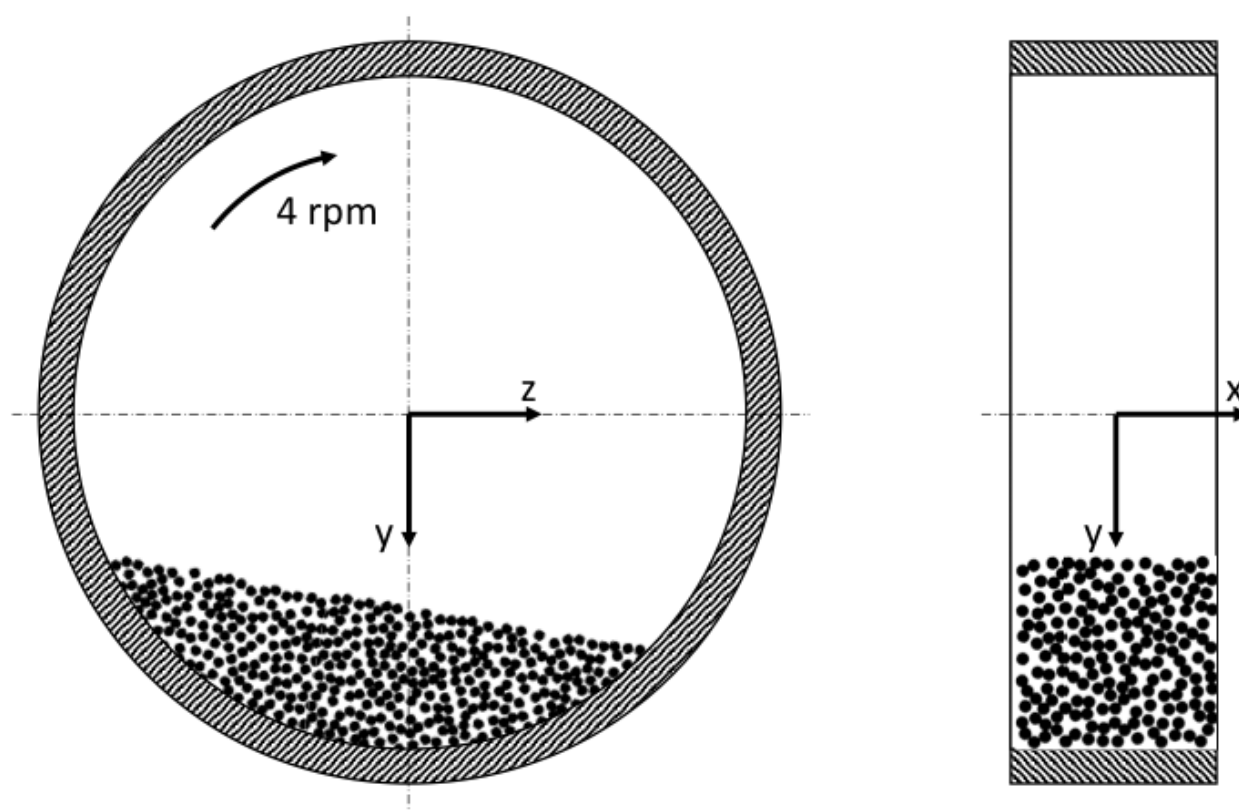

Fig. 2.   DEM domain.

3.1.1. Particles flow

The linear and angular accelerations of each particle are calculated by applying Newton's laws of motion, then position and orientation are updated by integration. Each particle is subject to: the gravitational force, which is calculated according to the mass densities of the constituting species; contact forces due to the mechanical interactions with neighbors and/or boundaries, which include viscous and elastic components in both the normal and shear direction, more details are provided in [51]; a drag force F_{drag} from the surrounding fluid, whose analytical expression is detailed in Section 3.4.

3.1.2. Conductive and radiative heat exchange between particles

Each i-particle exchanges heat with every other j-particle that is comprised within the cutoff distances for conduction and radiation. Conductive and radiative heat exchanges are calculated according to Eq. (1) and Eq. (2), respectively. Here $V_{(i \rightarrow j)}$ and A_c are the reciprocal view factor and the contact area, their expressions are retrieved from [52] and reported in Eq. (3) and Eq. (4), respectively.

$$\dot{q}_{i,cond} = \sum_{j=1}^{N} A_{c,ij} \frac{1}{1/k_i + 1/k_j} \frac{T_{p,i} - T_{p,j}}{\Delta x_{ij}} \tag{1}$$

$$\dot{q}_{i,rad} = \sum_{j=1}^{M} A_i V_{(i \rightarrow j)} \sigma \left(T_{p,i}^4 - T_{p,j}^4 \right) \tag{2}$$

$$V_{(i \rightarrow j)} = \frac{A_i}{\sum_{j=1}^{M} A_j} \tag{3}$$

$$A_{c,ij} = \frac{1}{2} \left[\left(R_i tan(5°) \right)^2 + \left(R_j tan(5°) \right)^2 \right] \tag{4}$$

In Eq. (2) the emissivity is set to 1, therefore no reflections occur. The assumption greatly simplifies the computation and stands for all the species involved in the present study.

3.1.3. Heat and mass transport inside particles

Each particle may be composed by solid, liquid and gaseous phase. Thermal equilibrium is assumed inside the particle meaning $T_p(r)$, being r the radial coordinate, is the same for all the different phases [53]. The assumption is justified by the negligible heat capacity of the gas phase compared to the liquid and solid. Hence, the heat transported through bulk movement of the gaseous species within the pore space can be neglected. Heat and mass transport within a particle are described by a set of one-dimensional/transient differential equations, as well as the state equation for the gaseous phase.

Eq. (5) expresses the mass conservation of a gaseous specie i. For a solid or liquid specie, the convective and diffusive terms vanish and Eq. (5) reduces to an ordinary differential equation, so no boundary conditions apply. ω_k is the production or consumption rate consequent to the chemical conversion k and M is the molar mass. The conservation of momentum of the gaseous phase is reported in Eq. (6) and it is obtained by applying the Darcy's law, for which a hypothesis of laminar flow within the particle is assumed considering the small size scale: here K_p identifies the so-called permeability coefficient, which characterizes the morphology of the porous space. The energy equation is based on the homogeneous model for a porous medium as described in [54] and reported in Eq. (7), where H_k denotes the enthalpy of the reaction k. k_{eff} is the effective thermal conductivity whose expression is reported in Eq. (8): here the summation is over all the solid species and k_{rad} accounts for the radiation of the porous space, more details are provided in [53]. Symmetry boundary conditions are imposed to Eq. (5) and Eq. (7) at $r = 0$. The respective boundary conditions at $r = R$ are stated in Eq. (9) and Eq. (10). Here α and β_i are the heat and mass transfer coefficients, respectively, with the subscript i referring to the correspondent gaseous specie of Eq. (5). The analytical expressions of the transfer coefficients are detailed in Section 3.4.

$$\frac{\partial (\rho_i)}{\partial t} + \frac{1}{r^2} \frac{\partial}{\partial r} \left(r^2 \rho_i u_g \right) = \frac{1}{\varepsilon_p} \frac{1}{r^2} \frac{\partial}{\partial r} \left(r^2 D_i \frac{\partial \rho_i}{\partial r} \right) + \sum_k M_i \omega_{k,i} \tag{5}$$

$$-\frac{\partial}{\partial r} \left(\varepsilon_p p_g \right) = \frac{\mu_g \varepsilon_p}{K_p} u_g \tag{6}$$

$$-\frac{\partial T_p}{\partial t} = \frac{1}{r^2}\frac{1}{\rho_p c_p}\frac{\partial}{\partial r}\left(r^2 k_{eff}\frac{\partial T_p}{\partial r}\right) + \frac{1}{\rho_p c_p}\sum_k \omega_k H_k \tag{7}$$

$$k_{eff} = \varepsilon_p k_g + \sum_i \xi_i k_i + k_{rad} \tag{8}$$

$$-D_i \frac{\partial \rho_i}{\partial r}\bigg|_{r=R_p} = \beta_{p,i} A_p (\rho_i - \rho_{f,i}) \tag{9}$$

$$-A k_{eff}\frac{\partial T_p}{\partial r}\bigg|_{r=R_p} = \dot{q}_{p,cond} + \dot{q}_{p,rad} + \alpha_p A_p (T_p - T_f) \tag{10}$$

3.1.4. Chemical conversion of particles

According to [55], kinetics of the chemical reactions involved in clinker forming are controlled by solid-state diffusions. In particular, the following mechanisms are identified: surface diffusion; joint diffusion; lattice diffusion. The latter is recognized as the slowest, so it is the one that effectively controls the rates of the reactions, with a temperature dependency of the diffusion coefficient of the Arrhenius-type. Further, all the reactions are assumed irreversible, coherently with [24].

Under these hypotheses, the rate of a generic k-reaction is a function of the molar concentrations of the reactants (solid, liquid or gaseous) as reported in Eq. (11) and the rate constant K, whose expression is shown in Eq. (12). In Eq. (11), n denotes the order of the reaction respect to the correspondent reactant and the product sequence is over all the reactants. In Eq. (12), a is the pre-exponential factor, E is the activation energy and R_{gas} is the gas constant.

$$\omega_k = K_k \prod_i C_i^{n_i} \tag{11}$$

$$K_k = a\, exp\left(\frac{-E}{R_g T_p}\right) \tag{12}$$

Table 2 summarizes the reactions considered in the present study with their activation energies, pre-exponential factors and enthalpies, data retrieved from [24].

Table 2. Reactions involved in clinker sintering [24].

Reaction	Enthalpy (J/kg)	Pre-exp (1/s)	Act. En. (J/mol)
$CaCO_3 \rightarrow CaO + CO_2$	-1.66e6	4.55e31	7.81e5
$2CaO + SiO_2 \rightarrow C2S$	6.03e5	4.11e5	1.93e5
$3CaO + Al_2O_3 \rightarrow C3A$	3.7e4	8.33e6	1.94e5
$4CaO + Al_2O_3 + Fe_2O_3 \rightarrow C4AF$	1.09e5	8.33e8	1.85e5
$C2S + CaO \rightarrow C3S$	4.48e5	1.33e5	2.56e5

3.2. CFD Approach for the Freeboard Region

The CFD domain covers the whole freeboard region. The air-intake geometry is shown in Fig. 1. Here the primary and secondary air enter through the sections A_1 and A_2, respectively. Coal particles are transported through the primary flow. The area of A_2 has been adjusted, according to the intake flows and the measured speed at the exhaust. The simplified geometry respect to the real design of the burner introduces an approximation on the local flow conditions, which could affect the predictions even at large scale, since coal ignition and its rate of oxidation are affected by the rate of mixing of the primary and secondary flow in the region close to the burner. However, the area of A_1 and consequently the intake speed of primary air has been adjusted in order to match the real position of the flame. Consequently, the numerical representation is expected to keep an adequate level of accuracy for the most part of the CFD domain. A no-slip condition is set at the rotating wall and the internal pressure is imposed at the exhaust. Particles interactions are included locally, according to their positions respect to the CFD grid.

A RANS method is exploited for solving the CFD field, which is turbulent in the region close to the burner. The CFD grid includes a refinement there and is consistent with a grid-independence study, more details are provided in Section 4. Grids of similar magnitude have also been found adequate in [27–30, 33].

The fuel is constituted by coal particles and their transport is determined according to the CFD velocity, using a diffusive model similar to the one discussed in [56]. The rate of oxidation of a single particle ω_{fuel} is calculated according to the combustion model from [24] and reported in Eq. (13) to (15). The heat released is included in the energy equation through a heat source in the right-hand side.

$$\omega_{fuel,p} = K_{fuel} \cdot d_o \cdot C_{O2} \tag{13}$$

$$K_{fuel} = a_{fuel} \cdot exp\left(\frac{-E_{fuel}}{R_g T_g}\right) \tag{14}$$

$$d_o = \left(\frac{3D_{ox}}{R_{fuel}^2 k_{fuel}}\right) \Big/ \left(\frac{3D_{ox}}{R_{fuel}^2 k_{fuel}} + 1\right) \tag{15}$$

3.3. FDM Approach for the Rotating Wall

The heat equation is numerically solved on the rotating wall with an FDM approach. Neumann boundary conditions are imposed at both sides, in particular: the heat exchange coefficient due to the forced convection with the environment is set to 30 W/m2K, value taken from [33] and consistent with experimental studies [57]; the emissivity of the external shell is set to 0.8, value taken from [33]; the convective heat exchange coefficient with the CFD domain is calculated from the Prandtl number using the correlations for flows through pipes provided in [58]; the heat exchange with particles is included through Eq. (1) and Eq. (2), for which the wall is assumed as a particle with infinite radius.

3.4. Particles-gas mass, momentum and convective heat transfer

Particles interactions are accounted where they are located, using an unresolved approach [59]. Consequently, the CFD grid has a spatial resolution bigger respect to the characteristic size of the individual channels between the particles. The CFD porosity ε_f is calculated for each computation cell as the ratio between the void and total volume. The coupling terms $\dot{m}_{f,i}$, f_{drag} and $\dot{q}_f$ are included in the right-hand sides of the Navier-Stokes equations. These sources/sinks account for the species, momentum and convective heat transfer with the particles, respectively.

The expression of f_{drag} is reported in Eq. (16). Here K_{bed} and C_{bed} are calculated according to the characteristics of the packed bed, their expressions are retrieved from [54] and reported in Eq. (17) and Eq. (18). The drag force exerted on a i-particle is calculated according to Eq. (19), being N the total number of particles inside the computation cell and V_{cell} the volume of the cell.

$$f_{drag} = -\frac{\mu_f}{K_{bed}}\varepsilon_f^2 u_f - C_{bed}\varepsilon_f^3 \rho_f |u_f| u_f \tag{16}$$

$$K_{bed} = \frac{2R_p^2 \varepsilon_f^3}{150(1-\varepsilon_f)^2} \tag{17}$$

$$C_{bed} = \frac{1.75(1-\varepsilon_f)}{2R_p \varepsilon_f^3} \tag{18}$$

$$F_{drag,i} = \frac{f_{drag} V_{cell}}{N} \tag{19}$$

The sources/sinks $\dot{q}_f$ and $m_{f,i}$ are calculated according to Eq. (20) and Eq. (21), respectively, where the summation is over the total number N of particles inside the cell. The transfer coefficients are obtained from the Nusselt, Reynolds and Sherwood numbers of the fluid domain, as indicated in Eq. (22) and Eq. (23) and with the subscript i referring to a generic gaseous specie. The expression of the Nusselt number Nu is reported in Eq. (24) and has been resumed from [60]. The particle Reynolds number Re_p and the hydraulic Reynolds number Re_h are expressed by Eq. (25) and Eq. (26), respectively: the first uses the particle diameter as the characteristic length scale, whilst the second accounts for the packing fraction of the particles bed, also. Substitution of Nusselt by Sherwood number, Prandtl by Schmidt number and the thermal conductivity by the gas diffusion coefficient allows determining the Sherwood number accordingly.

$$\dot{q}_f = \sum_{j=1}^{N}\langle\frac{A_j}{V_{cell}}\alpha(T_j - T_f)\rangle \tag{20}$$

$$\dot{m}_{f,i} = \sum_{j=1}^{N}\langle\frac{A_j}{V_{cell}}\beta_i(\rho_{j,i} - \rho_{f,i})\rangle \tag{21}$$

$$\alpha = Nu \frac{k_f}{2R_p} \tag{22}$$

$$\beta_i = Sh \frac{D_i}{2R_p} \tag{23}$$

$$Nu = \left[\left(1.18 \, Re_p^{0.58} \right)^4 + \left(0.23 \, Re_h^{0.75} \right)^4 \right]^{1/4} \tag{24}$$

$$Re_p = \frac{\rho_f \varepsilon_b |u_f| D_p}{\mu_f} \tag{25}$$

$$Re_h = \frac{Re_p}{1 - \varepsilon_f} \tag{26}$$

Fluid-to-particles heat and mass transfers are accounted through the boundary conditions stated in Eq. (9) and Eq. (10). Particles sharing their volume with different computation cells are handled according to the algorithm described in [61].

3.5. Particles-gas-wall radiative heat transfer

Radiative heat transfers are included through the resistance network shown in Fig. 3. Here the radiating temperatures for gas and wall are taken as the mean values on the yz-plane. The radiating temperature of the material bed is the mean temperature of the particles in the active layer, which are identified using their velocities. The emissivity values are set to 0.2 for the gas and 1 for the wall and particles, values taken from [24]. The emitting surfaces are $A_3 + A_4$, A_3 and A_4 for the gas, the wall and the material bed, respectively. Gas-wall and gas-material transfer occur through the areas A_3 and A_4, respectively, and the correspondent view factors are calculated accordingly. Analogously, the exposed wall and particles exchange radiative heat through the gas (whose absorbance is equal to the emissivity) with a view factor of 1. The net gas- and wall-particles transfer are split between all the particles that are located in the active layer and included into the right-hand sides of Eq. (9) and Eq. (10).
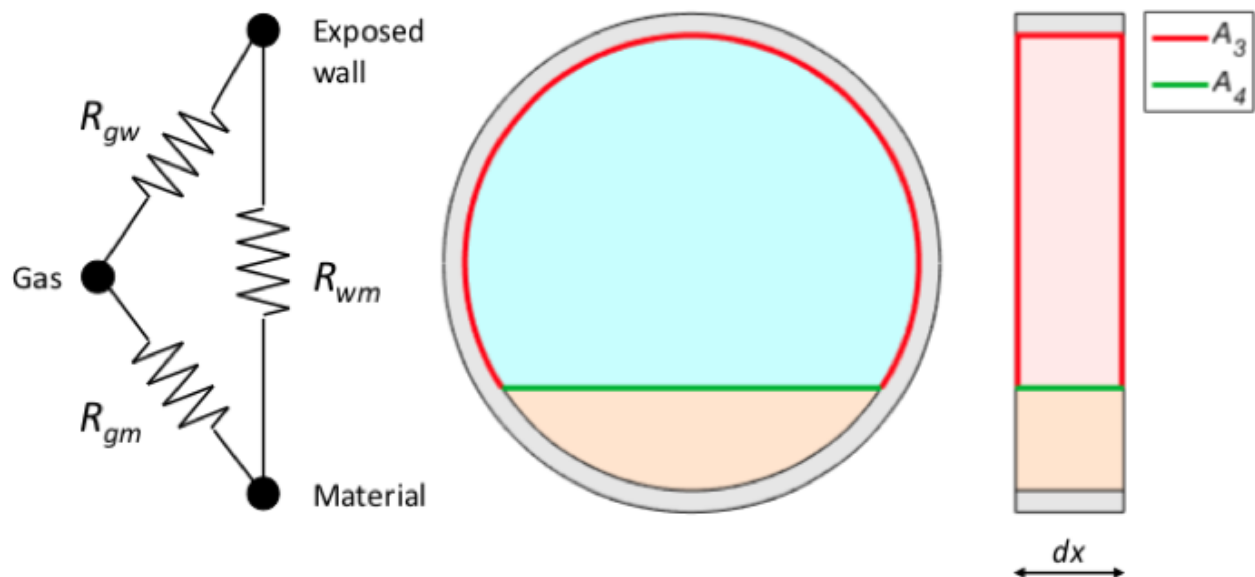

Fig. 3.   Resistance network for radiative heat transfers.

Initial and boundary conditions of the model are summarized in Table 3, for sake of clarity. The full list of assumptions is reported in Table 4.

Table 3.   Initial and boundary conditions.

Initial conditions		
Domain	**Variable**	**IC**
DEM	Temperature	Uniform 1220 K
DEM	x-velocity	Uniform 0.045 m/s
DEM	yz-velocity	Uniform 0 m/s
CFD	Temperature	Uniform 950 K
CFD	x-velocity	Uniform -12 m/s
CFD	yz-velocity	Uniform 0 m/s
Boundary conditions		
Domain	**Variable**	**Boundary**	**BC**
DEM	Temperature	Periodic boundaries	Adiabatic
DEM/Wall	Temperature	Powder-Immersed wall	Cond. heat transfer
DEM/Wall	Temperature	Powder-Exposed wall	Rad. heat transfer
DEM/CFD	Temperature	Powder-Gas	Conv./Rad. heat transfer
CFD/Wall	Temperature	Gas-Exposed wall	Conv./Rad. heat transfer
Wall	Temperature	External wall	Conv. heat transfer
CFD	Temperature	Intake A_1	273 K
CFD	Temperature	Intake A_2	950 K
CFD	Pressure	Exhaust	1.01e5-200 Pa
CFD	Velocity	Intake A_1	25 m/s
CFD	Velocity	Intake A_2	12 m/s
CFD	Velocity	Wall	No slip

Table 4.   Assumptions of the model.

Domain	Assumption
DEM	Emissivity set to 1
DEM	Thermal equilibrium inside particles
DEM	Arrhenius-type reaction constants
DEM	Irreversible reactions
DEM	Adiabatic BCs at periodic boundaries
CFD	Simplified geometry of intake
Powder/Wall/CFD	Simplified resistance network for rad. heat transfers

4. Numerical Strategy

The DEM domain ideally and uniformly moves along the x-direction at a constant speed of 0.045 m/s, which provides the expected residence time. The quasi-2D DEM domain is converted into 3D by shifting the thin slice along the x-direction at consecutive times. The coupling between the three domains is obtained with the following iteration scheme, which has been taken from [33]: 1) initialization, i.e. DEM run with no heat, mass and momentum transfer; 2) step 1, i.e. CFD-wall computation until steady state, by using last DEM solution; step 2, i.e. DEM computation by using the last CFD-wall solution; 3) iteration of steps 1 and 2 until convergence, which is verified by using the mean temperature of the wall T_{w_mean} at the internal nodes as done in [33]. More in detail, a default of ten iterations are performed initially; subsequently, at each n-iteration an error is computed as follows:

$$\text{error}(n) = 100 \cdot \frac{T_{w\_mean}(n) - mean[T_{w\_mean}(n-10:n)]}{mean[T_{w\_mean}(n-10:n)]} \tag{27}$$

being $mean[T_{w\_mean}(n-10:n)]$ mean of T_{w_mean} over the last ten iterations; convergence is assumed once error goes below a predefined threshold. DEM computation is the main bottleneck for computing speedup, due to the time step imposed for the explicit contact detection. Having reduced the whole powder region to a quasi-2D domain is effective in decreasing the time-to-solution to the length scale of hours.

Further improvements can be attained by assuming that particles flow is not affected by their thermochemical conversion: this is likely to be true for the present case, considering that the negligible LOI provides conservation of mass and moment of inertia for each particle. Under this assumption, one flow simulation could be exploited for running multiple thermochemical analyses, each one requiring less than one hour on a multi-core workstation. The time requirement is taken as acceptable for quasi-real-time monitoring, considering the large-scale dynamics of the process.

5.   Error Analysis

According to [62], errors and uncertainties are introduced in the various steps of a computational simulation i.e.: 1) conceptual modeling of the physical system; 2) mathematical modeling of the conceptual model; 3) discretization and algorithm selection for the mathematical model; 4) computer programming of the discrete model; 5) numerical solution of the computer program model; 6) representation of the numerical solution. These errors sum up and affect the final results, which therefore must be considered in view of the present considerations.

To the first two steps it can be referred the usage of a lumped resistance network for representing the radiative heat transfers. The simplification entails an error which is mostly due to a lower emitting temperature of the gas respect to the actual value with a maximum delta of about 80 degrees and a consequent estimated error of 10% on the assessment of the heat fluxes. This error overcomes all others therefore can be assumed as the limit of accuracy of the results.

DEM and CFD integration schemes belong to the third step. The first is explicit and based on the forward Euler method therefore only conditionally stable. The error is proportional to the integration step, which is chosen small enough to properly resolve the mechanical contacts between particles as detailed in Section 5.1. Considering the small time-scale of collisions respect to the thermochemical conversions, the numerical stability for integration of equations 5, 7 and 11 is automatically satisfied e the correspondent errors are negligible. Stability and error for particle dynamics are discussed in Section 5.1.

CFD integration is implicit and based on the Crank-Nicholson method. The discretization error is quantified through grid independence study with the local Courant number near the burner progressively reduced from 0.5 to 0.1 and a consequent variation of the maximum predicted temperature of 2%.

The iteration scheme belongs to steps 4 and 5. Threshold for the convergence criteria is set at 2%, based on a compromise between accuracy and the time requirement for computation.

6.   Results

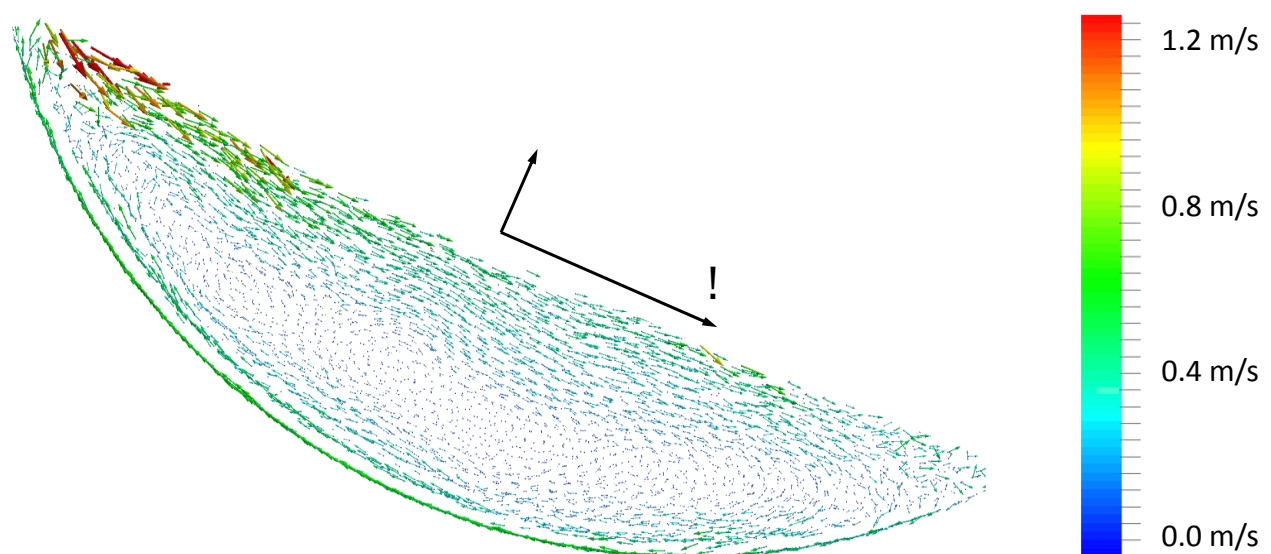### 6.1. Particles Flow

Fig. 4.   Particles velocities.

A prediction of the velocity distribution is shown in Fig. 4. Here the rolling mode of the material bed is evident. Indeed, as typical to this kind of operation, two zones can be identified: the passive region, where the particles move almost as a rigid body following the rotation of the wall, with the speed that linearly decreases towards the center; the active layer on the top, where particles slip over the free surface of the material bed. As a consequence of such movement, a continuous recirculation of the external particles takes place, whereas the internal ones are trapped in the bulk zone. The thickness of the active layer can be computed from the velocity profile along the radial direction of the kiln section and its trend as a function of the ξ-coordinate is reported in Fig. 5. The model is consistent with others from literature like the one discussed in [15] (input data reported in Table 5) whose prediction for the active layer is shown in Fig. 5, as well: as it can be seen, the latter provides a maximum thickness of the active layer of 0.16 m and an average speed of the particles inside the active layer of 0.9 m/s and the values are matched quite accurately by the present simulation (0.19 m and 0.8 m/s, respectively). The slight under-estimation of speed from XDEM can be explained with a higher energy dissipation due to having reduced the Young's modulus, which makes the viscous component of the contact force more relevant respect to the elastic one. The overestimation of the thickness is the consequence of the lower speed and conservation of mass. Indeed, DEM methods show a potential instability with hard materials because the usage of an explicit contact model could result in particles explosions if the contact is not properly resolved in time. In [63], the maximum time step for the computation stability is found to be $\Delta t_{min} = 0.14 \cdot sqrt(m_p/K_H)$, being K_H the Hertz stiffness. Assuming clinker particles, the formula entails a time step of 1e-4 s, which is largely smaller respect to the time scale of clinker manufacturing, i.e. the retention time. Therefore, the Young's modulus of clinker lumps has been reduced of a factor of 10 and the time step consequently increased to 1e-3 s.
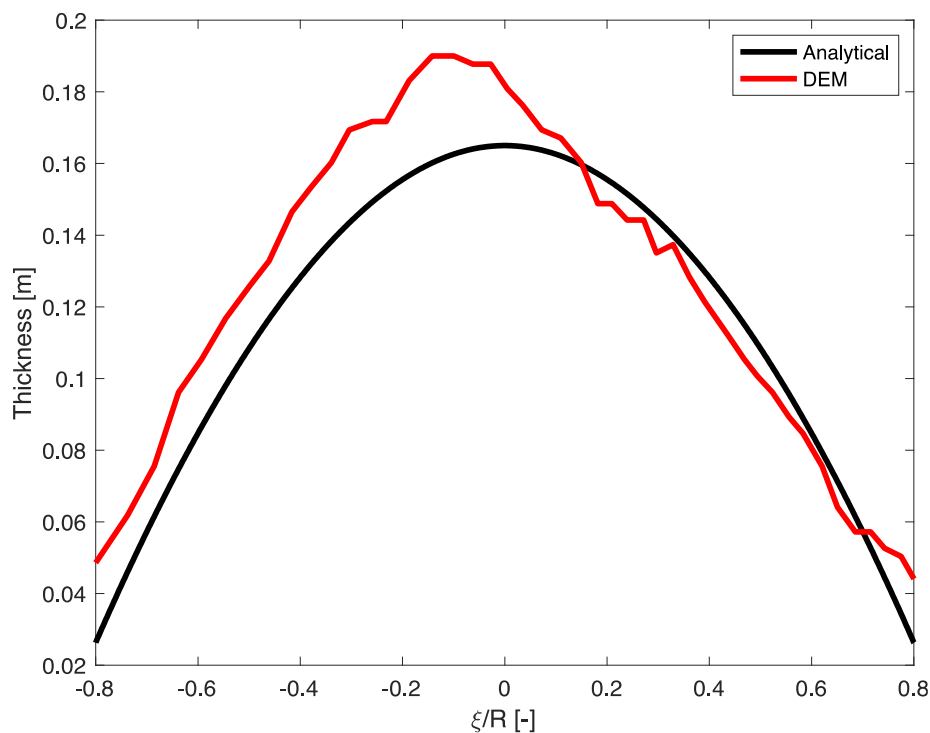

Fig. 5.   Comparison between DEM prediction and analytical model [15].

Table 5.   Inputs for analytical model [15].

Froude number	0.02
Drum diameter	2.1 m
Particles diameter	6 cm
Filling angle	57 deg
Dynamic contact angle	29 deg

6.2. Particles Heating and Conversion

While passing inside the kiln, the material undergoes a continuous heating. Using larger particles respect to the real ones (diameter of clinker lumps is around 0.01 m) is not expected to introduce relevant errors. Indeed, a total porosity $\varepsilon_t = \varepsilon_f + \varepsilon_p(1 - \varepsilon_f)$ as been used in Eq. (8). Particles in direct contact with the wall are heated by conduction, whilst those located on the top surface get heat by convection and radiation from the CFD domain and by radiation from the exposed wall. Adiabatic conditions are imposed at the periodic boundaries, the assumption is justified by the low thermal conductivity of the material bed.

Three different times are considered, which correspond to the positions of the DEM domain along the kiln shown in Fig. 1: 1 min after the material enters the kiln; 10 min, which is the time instant when the material is at the middle length of the kiln; 20 minutes, i.e. when the material exits the kiln.

Figure 6 shows the temperature distributions of the particles, on the yz-plane. At 1 min the temperature is still close to the initial value (1220 K). At 10 min the material reaches a mean temperature of 1423 K. At 20 min the mean temperature is equal to 1687 K. The velocity distribution affects the temperature of the particles: those on the top layer of the material bed, which are directly exposed to the gas and the upper wall, show higher temperatures; the bulk particles are at a lower temperature, because they get heat only by conduction from the outer particles. The standard deviation continuously increases from 0.96 K at 1 min to 5.1 K at 20 min and its trend along the kiln can be well appreciated in Fig. 7, together with a comparison against measurements.
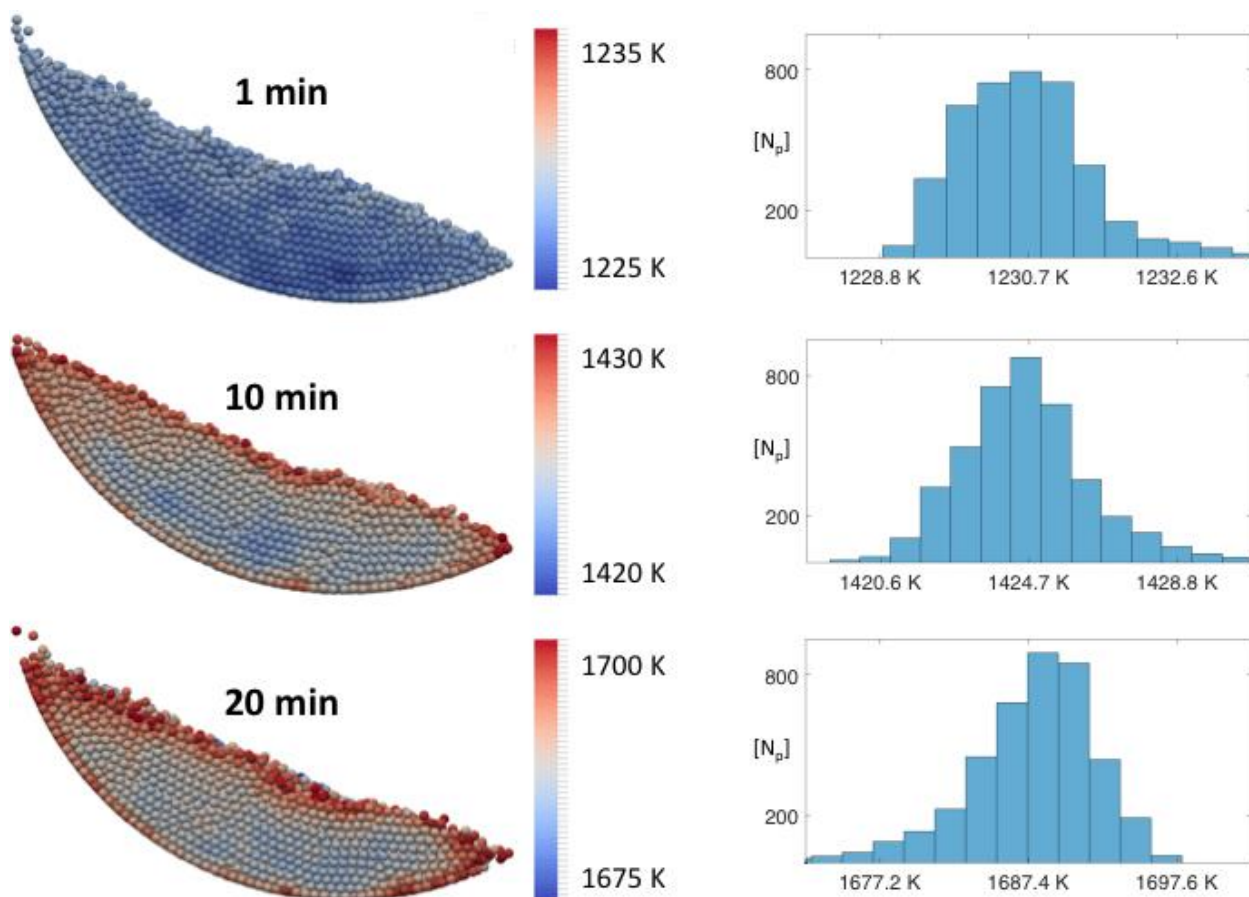

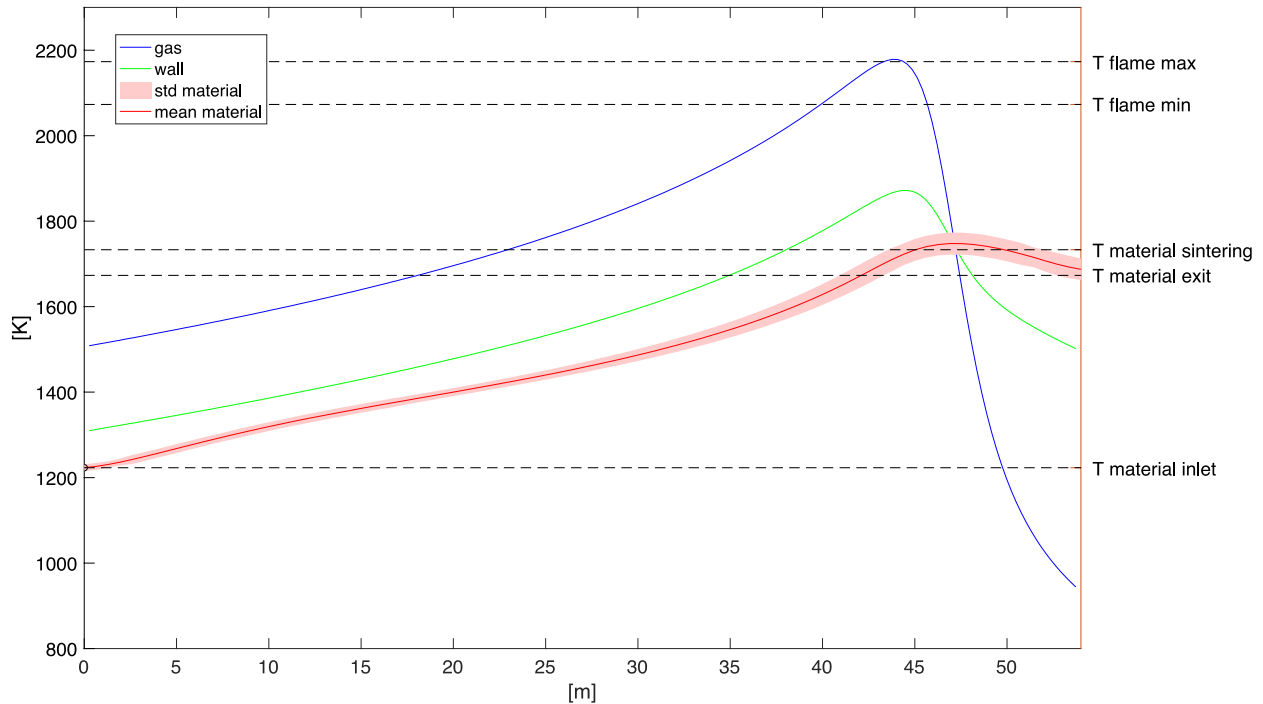Fig. 6.   Temperature of particles at different times and histograms of the respective distributions.

Fig. 7.   Temperature profiles.

Temperature of the particles drives their chemical conversion, until final clinker is obtained. Figure 8 shows the mass fractions of CaO on the yz-plane. CaO decomposition is accelerated in the outer particles, which are at a higher temperature respect to the others. Whilst at 1 min the chemical composition is almost uniform, at 10 min a slight gradient inside the material bed is evident. Similarly, at 20 min some unreacted CaO is still present inside the bulk particles. The mass fractions of C2S and C3S show specular distributions, with higher rates of conversion in the outer particles. Mean values at 20 min (0.15 for C2S and 0.60 for C3S) are in agreement with the composition reported from the production plant.
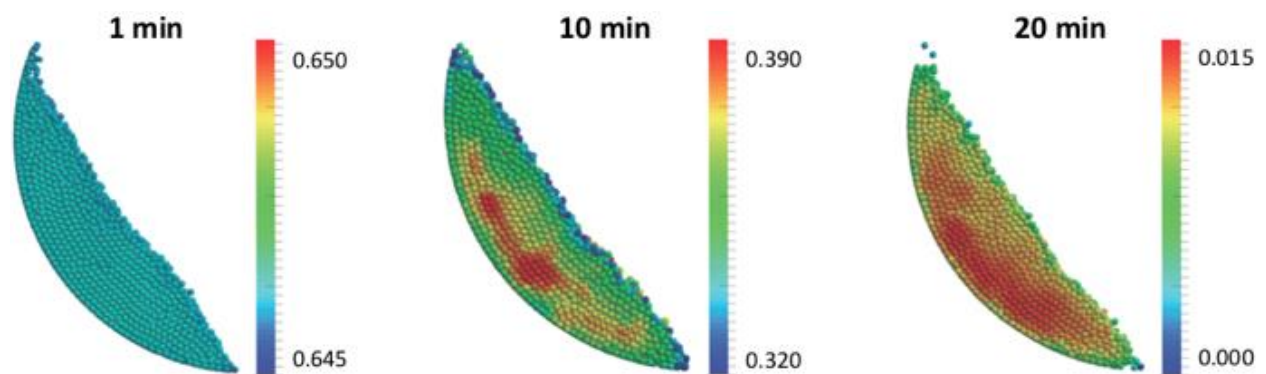

Fig. 8.   CaO mass fractions at different times.

6.3. CFD Domain and Wall

Figure 9 shows the numerical predictions of the CFD domain. The x-temperature trends i.e. the values averaged on the yz-plane can be appreciated in Fig. 7. Some considerations follow:
   1.   The simplified geometry of the burner helps reducing the computational burden but could affect the numerical prediction of the flame. However, the predicted temperature (2200 K) is consistent with the real data, as well its position, which starts from about 10 m downstream respect to the intake. The predicted time for complete coal burnout is around 1.5 s and compatible with the real

experience. Therefore, the error is eventually limited to the local region near the burner and the rest of the CFD representation is expected to be accurate enough.

2. The hot gas exchanges heat with the countercurrent material and the rotating wall. As a result, its temperature decreases towards the exhaust and uniforms through the *yz*-plane at a mean value of 1500 K. The same happens for the *x*-velocity, with a mean value at the exhaust of about 15 m/s.

3. It is worth to mention the inversion of the heat fluxes at the exit of the kiln, with the temperature of the material exceeding that of the wall and in turn of the gas. The same effect is found in [33].
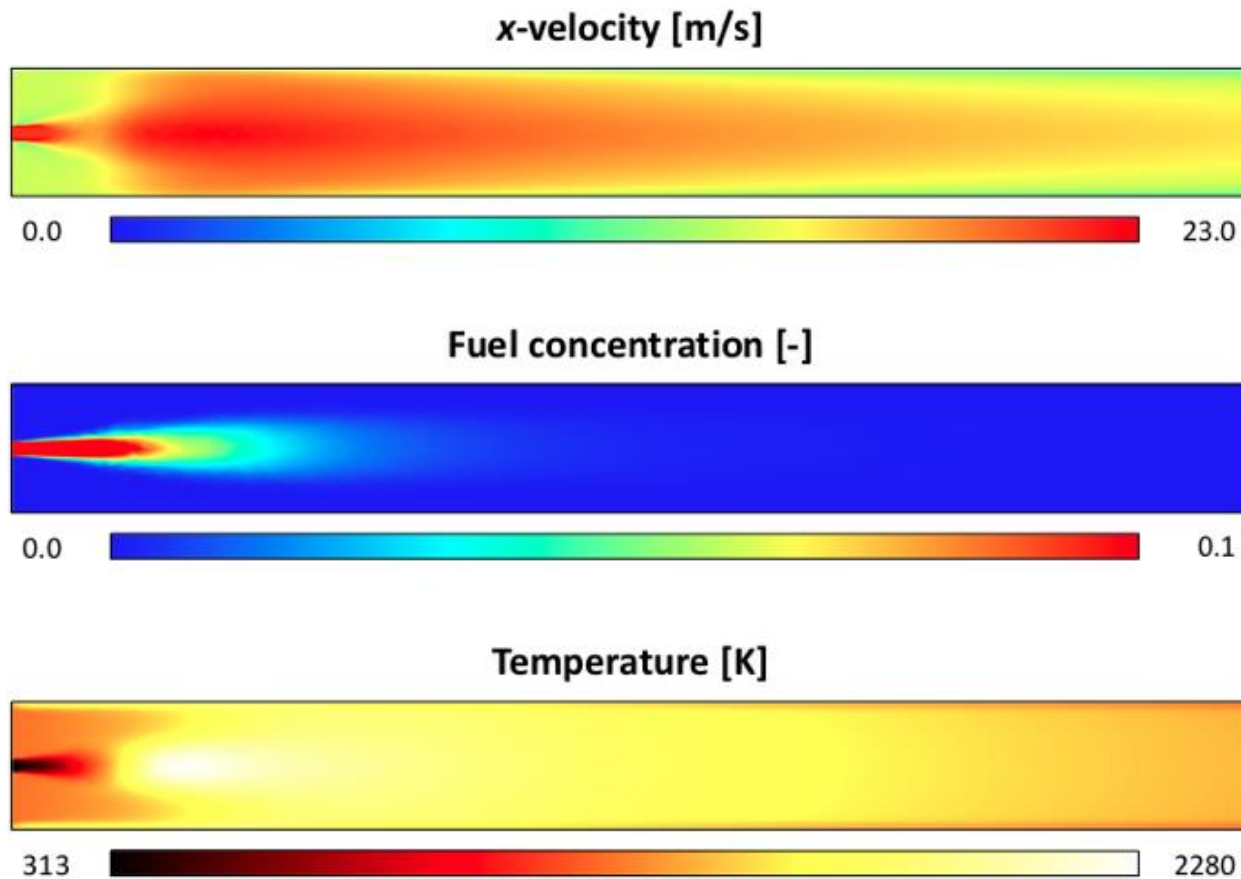

Fig. 9.   Predictions of the CFD domain.

Figure 10 shows the porosity and the local convective heat transfer coefficient between the CFD domain and the particles. The first is uniformly equal to 1 except where the particles are located. An analogous distribution can be observed for the second, with values different from zero only in the CFD cells that contain at least one particle.
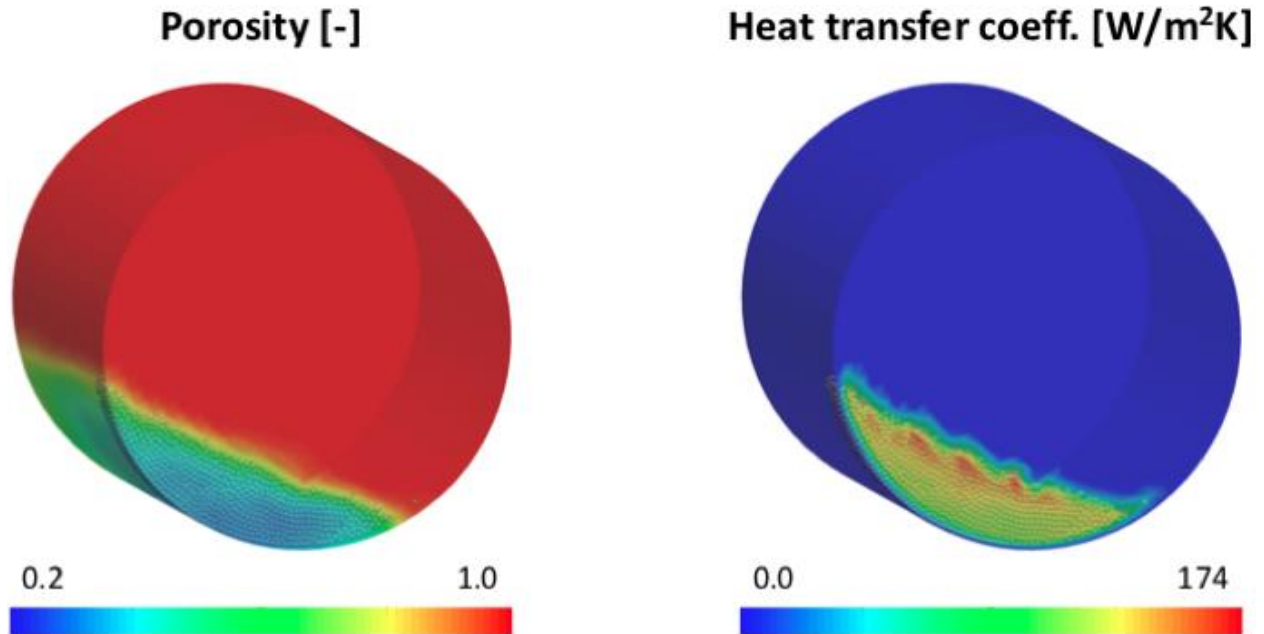
Fig. 10. Coupling between CFD domain and DEM domain.

7. Conclusions

In the present contribution, the XDEM method was applied to predict the thermochemical phenomena occurring in a rotary kiln for clinker production. The integration of the DEM approach for the particles with a CFD for the fluid domain allowed an accurate representation of the conductive and radiative heat exchanges between the particles and their chemical conversion, as well as the heat transfers between the fluid domain, the particles and the rotating wall. The motion of the particles was predicted, finding that the velocity distribution in a rolling mode-operated kiln affects the propagation of heat inside the material bed, producing a distribution of properties in the final product.

The thermochemical results were validated by using real data from the production plant. A comparison with literature data demonstrated the effectiveness of the model in providing an accurate representation of the advective mass transport phenomena, therefore of the local heat redistribution within the material bed. In general, the consistency of the predictions respect to the benchmark data proved the effectiveness of an integrated CFD-DEM method in simulating thermal processes involving gases and powder materials.

The time-effective computation methodology could allow the exploitation of XDEM as the theoretical basis in quasi-real-time applications like indirect monitoring and model-based control.

Acknowledgements

Nomenclature

Unless stated otherwise.

Letters/Greek letters									
A	Surface area	a	Pre-exp. factor	C	Mass concentration	c	Specific heat	D	Diffusion coefficient
H	Enthalpy of reaction	h	Enthalpy state variable	k	Thermal conductivity	p	Pressure	R	Radius
T	Temperature	u	Velocity	V	Volume	α	Conv. heat transf. coeff.	β	Specie transfer coeff.
ε	Porosity	ϵ	Emissivity	μ	Dynamic viscosity	ρ	Mass density	ω	Rate of reaction
Subscripts									
f	Fluid CFD	fu	Fuel	g	Gas phase particle	ox	Oxygen	p	Particles

References

[1] European Integrated Pollution Prevention and Control Bureau (EIPPCB), "Best Available Techniques (BAT) Reference Document for the Production of Cement, Lime and Magnesium Oxide," 2013. doi: 10.2788/12850

[2] A. A. Boateng, *Rotary Kilns: Transport Phenomena and Transport Processes*, 2nd ed. Butterworth-Heinemann, 2015.

[3] K. D. Stephan, J. A. Pearce, L. Wang, and E. Ryza, "Cement kiln temperature measurements using microwave radiometry," in *Proceedings of the IEEE MTT-S International Microwave Symposium Digest*, Long Beach, California, USA, 12-17 June 2005. doi: 10.1109/MWSYM.2005.1516545

[4] A. Atmaca and R. Yumrutas, "Analysis of the parameters affecting energy consumption of a rotary kiln in cement industry," *Applied Thermal Engineering*, vol. 66, pp. 435-444, 2014. doi: 10.1016/j.applthermaleng.2014.02.038

[5] M. Schneider, M. Romer, M. Tschudin, and H. Bolio, "Sustainable cement production—Present and future," *Cement and Concrete Research*, vol. 41, pp. 642-650, 2011. doi: 10.1016/j.cemconres.2011.03.019

[6] P. Khongprom and U. Suwanmanee, "Environmental benefits of the integrated alternative technologies of the Portland Cement Production: A case study in Thailand," *Engineering Journal*, vol. 21, pp. 15-27, 2017. doi: doi.org/10.4186/ej.2017.21.7.15

[7] P. Kadlec, B. Gabrys, and S. Strandt, "Data-driven soft sensors in the process industry," *Computers & Chemical Engineering*, vol. 33, pp. 795-814, 2009. doi: 10.1016/j.compchemeng.2008.12.012

[8] D. E. Seborg, T. F. Edgar, D. A. Mellichamp, and F. J. III Doyle, *Process Dynamics and Control*. John Wiley & Sons Inc, 2010.

[9] A. A. Boateng and V. Barr, "Granular flow behavior in the transverse plane of a partially filled rotating cylinder," *Journal of Fluid Mechanics*, vol. 330, pp. 233-249, 1997. doi: 10.1017/S0022112096003680

[10] T. Kawaguchi, "MRI measurement of granular flows and fluid-particle flows," *Advanced Powder Technology*, vol. 21, pp. 235-241, 2010. doi: 10.1016/j.apt.2010.03.014

[11] D. A. Santos, M. A. S. Barrozo, C. R. Duarte, F. Weigler, and J. Mellmann, "Investigation of particle dynamics in a rotary drum by means of experiments and numerical simulations using DEM," *Advanced Powder Technology*, vol. 27, pp. 692-703, 2016. doi: 10.1016/j.apt.2016.02.027

[12] S. H. Chou, H. J. Hu, and S. S. Hsiau, "Investigation of friction effect on granular dynamics behaviour in a rotating drum," *Advanced Powder Technology*, vol. 27, pp. 1912-1921, 2016. doi: 10.1016/j.apt.2016.06.022

[13] D. J. Parker, A. E. Dijkstra, T. W. Martin, and J. P. K. Seville, "Positron emission particle tracking studies of spherical particle motion in rotating drums," *Chemical Engineering Science*, vol. 52, pp. 2011-2022, 1997. doi: 10.1016/S0009-2509(97)00030-4

[14] A. A. Boateng, "Boundary layer modeling of granular flow in the transverse plane of a partially filled rotating cylinder," *International Journal of Multiphase Flow*, vol. 24, pp. 499-521, 1998. doi: 10.1016/S0301-9322(97)00065-7

[15] X. Y. Liu, E. Specht, O. G. Gonzalez, and P. Walzel, "Analytical solution for the rolling-mode granular motion in rotary kilns," *Chemical Engineering and Processing: Process Intensification*, vol. 45, pp. 515-521, 2006. doi: 10.1016/j.cep.2005.10.009

[16] M. Yamamoto, S. Ishihara, and J. Kano, "Evaluation of particle density effect for mixing behavior in a rotating drum mixer by DEM simulation," *Advanced Powder Technology*, vol. 27, pp. 864-870, 2016. doi: 10.1016/j.apt.2015.12.013

[17] R. K. Soni, R. Mohanty, S. Mohanty, and B. K. Mishra, "Numerical analysis of mixing of particles in drum mixers using DEM," *Advanced Powder Technology*, vol. 27, pp. 531-540, 2016. doi: 10.1016/j.apt.2016.01.016

[18] N. Gui, X. Yang, J. Tu, and S. Jiang, "Numerical study of the motion behaviour of three-dimensional cubic particle in a thin drum," *Advanced Powder Technology*, vol. 29, pp. 426-437, 2018. doi: 10.1016/j.apt.2017.11.033

[19] S. Yang, K. Luo, M. Fang, J. Fan, and K. Cen, "Discrete element study of solid circulating and resident behaviors in an internally circulating fluidized bed," *Chemical Engineering Journal*, vol. 248, pp. 145-157, 2014. doi: 10.1016/j.cej.2014.03.032

[20] G. J. Finnie, N. P. Kruyt, M. Ye, C. Zeilstra, and J. A. M. Kuipers, "Longitudinal and transverse mixing in rotary kilns: A discrete element method approach," *Chemical Engineering Science*, vol. 60, pp. 4083-4091, 2005. doi: 10.1016/j.ces.2004.12.048

[21] Z. Xie and J. J. Feng, "Numerical analysis of behavior of active layer in rotary kilns by discrete element method," *Journal of Central South University*, vol. 20, pp. 634-639, 2013. doi: 10.1007/s11771-013-1529-4

[22] R. Y. Yang, A. B. Yu, L. McElroy, and J. Bao, "Numerical simulation of particle dynamics in different flow regimes in a rotating drum," *Powder Technology*, vol. 188, pp. 170-177, 2008. doi: 10.1016/j.powtec.2008.04.081

[23] A. A. Estupinan Donoso, "A discrete-continuous approach to model powder metallurgy processes," Ph.D. thesis, Université du Luxembourg, Luxembourg, 2016. Available: http://hdl.handle.net/10993/27324

[24] H. A. Spang, "A dynamic model of a cement kiln," *Automatica*, vol. 8, pp. 309-323, 1972. doi: 10.1016/0005-1098(72)90050-7

[25] K. S. Mujumdar and V. V. Ranade, "Simulation of rotary cement kilns using a one-dimensional model," *Chemical Engineering Research and Design*, vol. 84, pp. 165-177, 2006. doi: 10.1205/cherd.04193

[26] C. Csernyei and A. G. Straatman, "Numerical modeling of a rotary cement kiln with improvements to shell cooling," *International Journal of Heat and Mass Transfer*, vol. 102, pp. 610-621, 2016. doi: 10.1016/j.ijheatmasstransfer.2016.06.058

[27] N. C. Markatos, "Mathematical modelling of single and two-phase flow problems in the process industries," *Oil & Gas Science and Technology*, vol. 48, pp. 631-662, 1993. doi: 10.2516/ogst:1993036

[28] T. Avgeropoulos, J. P. Glekas, and C. Papadopoulos, "Numerical simulation of the combustion aerodynamics inside a rotary cement kiln," in *Energy Efficiency in Process Technology*, P. A. Pilavachi, Ed. Springer, 1993, pp. 767-778. doi: 10.1007/978-94-011-1454-7_68

[29] F. C. Lockwood, B. Shen, and T. Lowes, "Numerical study of petroleum coke fired cement kiln flames," in *Proceedings of the Third International Conference on Combustion Technologies for a Clean Environment*, Lisbon, Portugal, 3-6 July 1995.

[30] F. C. Lockwood and B. Shen, "Performance predictions of pulverised-coal flames of power station furnace and cement kiln types," *Symposium (International) on Combustion*, vol. 25, pp. 503-509, 1994. doi: 10.1016/S0082-0784(06)80679-X

[31] K. C. Karki, S. V. Patankar, and J. Grant, "Simulation of fluid flow, combustion and heat transfer in a coal-fired cement kiln," in *Proceedings of the 2000 ASME International Mechanical Engineering Congress*, Orlando, Florida, USA, 5-10 November 2000.

[32] T. P. Bhad, S. Sarkar, A. Kaushik, and S. V. Herwadkar, "CFD modeling of a cement kiln with multi channel burner for optimization of flame profile," in *Proceedings of the Seventh International Conference on CFD in the Minerals and Process Industries*, Melbourne, Australia, 9-11 December 2009.

[33] E. Mastorakos, A. Massias, C. D. Tsakiroglou, D. A. Goussis, V. N. Burganos, and A. C. Payatakes, "CFD predictions for cement kilns including flame modelling, heat transfer and clinker chemistry," *Applied Mathematical Modelling*, vol. 23, pp. 55-76, 1999. doi: 10.1016/S0307-904X(98)10053-7

[34] S. Wang, J. Lu, W. Li, J. Li, and Z. Hu, "Modeling of pulverized coal combustion in cement rotary kiln," *Energy Fuels*, vol. 20, pp. 2350-2356, 2006. doi: 10.1021/ef060027p

[35] K. S. Mujumdar and V. V. Ranade, "CFD modeling of rotary cement kilns," *Asia-Pacific Journal of Chemical Engineering*, vol. 3, pp. 106-118, 2008. doi: 10.1002/apj.123

[36] A. V. Luikov, "Systems of differential equations of heat and mass transfer in capillary-porous bodies (review)," *International Journal of Heat and Mass Transfer*, vol. 18, pp. 1-14, 1975. doi: 10.1016/0017-9310(75)90002-2

[37] T. Bluhm-Drenhaus, E. Simsek, S. Wirtz, and V. Scherer, "A coupled fluid dynamic-discrete element simulation of heat and mass transfer in a lime shaft kiln," *Chemical Engineering Science*, vol. 65, pp. 2821-2834, 2010. doi: 10.1016/j.ces.2010.01.015

[38] T. Swasdisevi, W. Tanthapanichakoon, T. Charinpanitkul, T. Kawaguchi, T. Tanaka, and Y. Tsuji, "Prediction of gas-particle dynamics and heat transfer in a two-dimensional spouted bed," *Advanced Powder Technology*, vol. 16, pp. 275-293, 2005. doi: 10.1163/1568552053750215

[39] C. B. Dinh, C. C. Liao, and S. S. Hsiau, "Numerical study of hydrodynamics with surface heat transfer in a bubbling fluidized-bed reactor applied to fast pyrolysis of rice husk," *Advanced Powder Technology*, vol. 28, pp. 419-429, 2017. doi: 10.1016/j.apt.2016.10.013

[40] A. H. Mahmoudi, F. Hoffmann, B. Peters, and X. Bessaron, "Numerical study of the influence of particle size and packing on pyrolysis products using XDEM," *International Communications in Heat and Mass Transfer*, vol. 71, pp. 20-34, 2016. doi: 10.1016/j.icheatmasstransfer.2015.12.011

[41] A. A. Estupinan Donoso, and B. Peters, "XDEM employed to predict reduction of tungsten oxide in a dry hydrogen atmosphere," *International Journal of Refractory Metals and Hard Materials*, vol. 49, pp. 88-94, 2015. doi: 10.1016/j.ijrmhm.2014.08.012

[42] A. A. Estupinan Donoso, F. Hoffman, and B. Peters, "eXtended Discrete Element Method used for convective heat transfer predictions," *International Review of Mechanical Engineering*, vol. 7, pp. 329-336, 2013.

[43] B. Peters, X. Besseron, A. A. Estupinan Donoso, F. Hoffmann, M. Michael, and A. Mahmoudi, "The extended discrete element method (XDEM) applied to drying of a packed bed," *International Flame Research Foundation Combustion Journal*, vol. 14, pp. 1-16, 2014. ISSN: 2075-3071.

[44] A. H. Mahmoudi, F. Hoffmann, and B. Peters, "Application of XDEM as a novel approach to predict drying of a packed bed," *International Journal of Thermal Sciences*, vol. 75, pp. 65-75, 2014. doi: 10.1016/j.ijthermalsci.2013.07.016

[45] E. Copertaro, P. Chiariotti, A. A. Estupinan Donoso, N. Paone, B. Peters, and G. M. Revel, "A discrete-continuous approach to describe $CaCO_3$ decarbonation in non-steady thermal conditions," *Powder Technology*, vol. 275, pp. 131-138, 2015. doi: 10.1016/j.powtec.2015.01.072

[46] E. Copertaro, P. Chiariotti, A. A. Estupinan Donoso, N. Paone, B. Peters, and G. M. Revel, "XDEM for tuning lumped models of thermochemical processes involving materials in the powder state," *Engineering Journal*, vol. 20, no. 5, pp. 187-201, 2016. doi: 10.4186/ej.2016.20.5.187

[47] G. Pozzetti and B. Peters, "A multiscale DEM-VOF method for the simulation of three-phase flows," *International Journal of Multiphase Flow*, vol. 99, pp. 186-204, 2018. doi: 10.1016/j.ijmultiphaseflow.2017.10.008

[48] M. Baniasadi, M. Baniasadi, and B. Peters, "Coupled CFD-DEM with heat and mass transfer to investigate the melting of a granualr packed bed," *Chemical Engineering Science*, vol. 178, pp. 136-145, 2018. doi: 10.1016/j.ces.2017.12.044

[49] M. Baniasadi and B. Peters, "Resolving multiphase flow through packed bed of solid particles using eXtended Discrete Element Method with porosity calculation," *Industrial & Engineering Chemistry Research*, vol. 56, pp. 11996-12008, 2017. doi: 10.1021/acs.iecr.7b02903

[50] P. C. Hewlett, *Lea's Chemistry of Cement and Concrete*, 4th ed. Elsevier Ltd., 2003.

[51] M. Michael, "A discrete approach to describe the kinematics between snow and a tire tread," Ph.D. thesis, Université du Luxembourg, Luxembourg, 2016. Available: http://hdl.handle.net/10993/18160

[52] B. Peters, *Thermal Conversion of Solid Fuels*. WIT Press, 2003.

[53] F. Hoffmann, "Modelling heterogeneous reactions in packed beds and its application to the upper shaft of a blast furnace," Ph.D. thesis, Université du Luxembourg, Luxembourg, 2014. Available: http://hdl.handle.net/10993/16663

[54] A. Faghri and Y. Zhang, *Transport Phenomena in Multiphase Systems*. Elsevier Academic Press, 2006.

[55] S. N. Ghosh, *Advances in Cement Technology: Critical Reviews and Case Studies on Manufacturing, Quality Control, Optimization and Use*. Elsevier, 2014.

[56] D. Hryb, M. Cardozo, S. Ferro, and M. Goldschmit, "Particle transport in turbulent flow using both Lagrangian and Eulerian formulations," *International Communications in Heat and Mass Transfer*, vol. 36, pp. 451-457, 2009. doi: 10.1016/j.icheatmasstransfer.2009.01.017

[57] H. Ma, W. Xia, W. Zhou, W. Liu, Z. Guo, C. Zhang, Y. Zhang, and N. Deng, "Experimental investigation on the steady, external laminar mixed convection heat transfer characteristics around a large diameter horizontal rotating cylinder," *International Communications in Heat and Mass Transfer*, vol. 57, pp. 239-246, 2014. doi: 10.1016/j.icheatmasstransfer.2014.08.006

[58] S. Whitaker, "Forced convection heat transfer correlations for flow in pipes, past flat plates, single cylinders, single spheres, and for flow in packed beds and tube bundles," *AIChE Journal*, vol. 18, pp. 361-371, 1972. doi: 10.1002/aic.690180219

[59] M. Vango, S. Pirker, and T. Lichtenegger, "Unresolved CFD-DEM modeling of multiphase flow in densely packed particle beds," *Applied Mathematical Modelling*, vol. 56, pp. 501-516, 2018. doi: 10.1016/j.apm.2017.12.008

[60] E. Achenbach, "Heat and flow characteristics of packed beds," *Experimental Thermal and Fluid Science*, vol. 10, pp. 17-27, 1995. doi: 10.1016/0894-1777(94)00077-L

[61] H. Xiao and J. Sun, "Algorithms in a robust hybrid CFD-DEM solver for particle-laden flows," *Communications in Computational Physics*, vol. 9, pp. 297-323, 2011. doi: 10.4208/cicp.260509.230210a

[62] W. L. Oberkampf, S. M. DeLand, B. M. Rutherford, K. V. Diegert, and K. F. Alvin, "Error and uncertainty in modeling and simulation," *Reliability Engineering and System Safety*, vol. 75, pp. 333-357, 2002. doi: 10.1016/S0951-8320(01)00120-X

[63] P. A. Cundall and O. D. L. Strack, "A discrete numerical model for granular assemblies," *Géotechnique*, vol. 29, pp. 47-65, 1979. doi: 10.1680/geot.1979.29.1.47

[64] S. Varrette, P. Bouvry, H. Cartiaux, and F. Feorgatos, "Management of an academic HPC cluster: The UL experience," in *Proceedings of the 2014 International Conference on High Performance Computing & Simulation*, Bologna, Italy, 21-25 July 2014, pp. 959-967. doi: 10.1109/HPCSim.2014.6903792